pp 449–468. © Royal Aeronautical Society 2017
doi: 10.1017/aer.2016.123

Robustness analysis on aerial deployment motion of a Mars aircraft using multibody dynamics simulation: effects of wing-unfolding torque and timing

Koji Fujita
fujita@flab.isas.jaxa.jp
Institute of Space and Astronautical Science
Japan Aerospace Exploration Agency
Sagamihara
Kanagawa
Japan

Hiroki Nagai
Department of Aerospace Engineering
Tohoku University
Sendai
Miyagi
Japan

ABSTRACT

This paper investigates the effects of the design variables of an aerial deployment mechanism on the robustness of the aerial deployment through a multibody dynamics simulation. The aircraft is modelled as three joined rigid bodies: a right wing, a left wing and a centre body. A spring-loaded hinge is adopted as an actuator for deployment. The design variables are the hinge torque and the deployment timing. The robustness is evaluated using a sigma level method. The margins for the safe deployment conditions are set for the evaluation functions. The dispersive input variables are the initial drop velocity, the surrounding gust velocity, the initial pitch angle and the initial height. The design point with a deployment torque scale value F of 0.7 and a right-wing deployment delay time T_{SR} of 1.0 s can safely deploy in the low-torque deployment condition. This design point is able to accomplish both a safe deployment and a lightweight deployment mechanism.

Keywords: aerial deployment; deployment mechanism; design; folding wing; Mars aircraft; multibody dynamics simulation; robustness

Received 8 July 2016; revised 22 December 2016; accepted 28 November 2016; first published online 16 January 2017.
This is an adaptation of a paper first presented at the 2015 Asia-Pacific International Symposium on Aerospace Technology in Cairns, Australia

NOMENCLATURE

A, B, C	rigid bodies
b	span
b_{A}	span of centre wing
b_{out}	span of section outwards from hinge
c	chord length
$C_{\mathrm{Dparachute}}$	drag coefficient of parachute
C_{lp}	rolling moment coefficient derivative by roll rate
C_{lr}	rolling moment coefficient derivative by yaw rate
$C_{L,W,max}$	maximum lift coefficient of main wing
C_{mq}	pitching moment coefficient derivative by pitch rate
C_{np}	yawing moment coefficient derivative by roll rate
C_{nr}	yawing moment coefficient derivative by yaw rate
C_{Yr}	side force coefficient due to yaw rate
DNS	direct numerical simulation
e	evaluation function
$E_{\mathrm{contributing}}$	evaluation functions contributing to total minimum sigma level
$E^*_{\mathrm{contributing}}$	evaluation functions contributing to minimum sigma level
F	deployment torque scale; ratio of torques between deployment mechanism and aerodynamic force
$F_{Z\mathrm{Aw}}$	z-direction force on wing of rigid body A
g	acceleration due to gravity
h	height
ID_{Disp}	identification number of the target dispersive input variable
ID_{Eval}	identification number of the target evaluation function
I_{XX}, I_{YY}, I_{ZZ}	moment of inertia
I_{XZ}	product of inertia
l	maximum lift force per unit wing span
LES	large eddy simulation
LSL	lower specification limit
m_{total}	total mass
$M_{b/2}$	bending moment on the centre of the main wing
$M_{\mathrm{Reac\ Req}}$	requirement of the hinge reaction moment
n	sigma level
n_{limit}	limit load factor
n_{min}	minimum sigma level
$n_{\mathrm{min\ Total}}$	total minimum sigma level
P, Q, R	angular rate
q	dynamic pressure
RANS	Reynolds-averaged Navier-Stokes equations
Re	Reynolds number
S_{out}	wing area of section outwards from hinge
$S_{\mathrm{parachute}}$	reference area of parachute
t	time
T_{aero}	torque on hinge due to aerodynamic forces
T_{deploy}	torque due to deployment mechanism
$T_{\mathrm{spring}\vert\mathrm{Dep}}$	torque of spring while wings are in deployed state

https://doi.org/10.1017/aer.2016.123 Published online by Cambridge University Press

T_{SL}	left wing deployment delay time
T_{SR}	right wing deployment delay time
U, V, W	translational velocity
USL	upper specification limit
$V_{\text{contributing}}$	dispersive input variables contributing to total minimum sigma level
V_{terminal}	terminal velocity
X, Y, Z	coordinates of centre body
X_0, Y_0, Z_0	inertial frame of reference
$\boldsymbol{x}$	dispersive input variables vector
Δ	difference for sensitivity calculation
θ_{dep}	deployment angle
μ_e	average of the evaluation function e
$\boldsymbol{\mu}_{\mathbf{x}}$	average vector of dispersive input variables
μ_{xi}	average of i-th dispersive input variable
ρ	atmospheric density
σ_e	standard deviation of evaluation function e
σ_{xi}	standard deviation of i-th dispersive input variable
φ, θ, ψ	Euler angle

1.0 INTRODUCTION

A deployment mechanism is one of the design solutions that satisfies the requirements for both large wing area and compactness. These properties are suitable for certain aircraft, such as an aircraft for Mars exploration, because the atmosphere is rare and the transportable volume is limited. In addition, the aerial deployment technique is suitable for such aircraft. It allows the elimination of landing/take-off gear and the utilization of an initial altitude. A simple, lightweight and reliable design of the deployment mechanism is required.

Types of deployment mechanisms include the folding type, the inflatable type, the extension type, etc. Extensive research is currently being carried out to study each type of deployment mechanism. A report by Jacob et al presents certain outlines of these deployment mechanisms and certain rudimentary restrictions regarding their design[1]. However, because the deployment techniques have still not yet matured, each design team has to design and study the type suitable for a Mars probe from scratch. Aircraft featuring aerial deployment techniques include the ARES, the AME and the FLYRT[2-4]. A number of aerial deployment processes have been adopted; however, the study of deployment techniques has only been a trial-and-error process based on flight tests and simulations of individual aircraft. As a consequence, neither the methods for the design of mid-air deployment mechanisms, nor the impacts of the design on the deployment behaviour have been clarified.

One of the important points of the design of the deployment mechanism is a dispersion of the deploying conditions such as the surrounding gust, drop velocity, attitude, height, etc. For example, it is known that extremely strong prevailing westerly winds blow in the Martian sky, and that their speeds vary seasonally and daily[5]. Rafkin and Michaels[6] present the simulation results of the wind speed in valleys and in craters of Mars, as well as the weather predictions at the landing site of the Mars rover. It includes an estimate of the maximum wind speed, which is 50 m/s at an altitude of 12.4 km at the Gusev Crater near the Martian equator. It also estimates that the maximum wind speed near the ground surface of the Gusev Crater is 20 m/s. A variation in conditions during aerial deployment may change the dynamic

https://doi.org/10.1017/aer.2016.123 Published online by Cambridge University Press

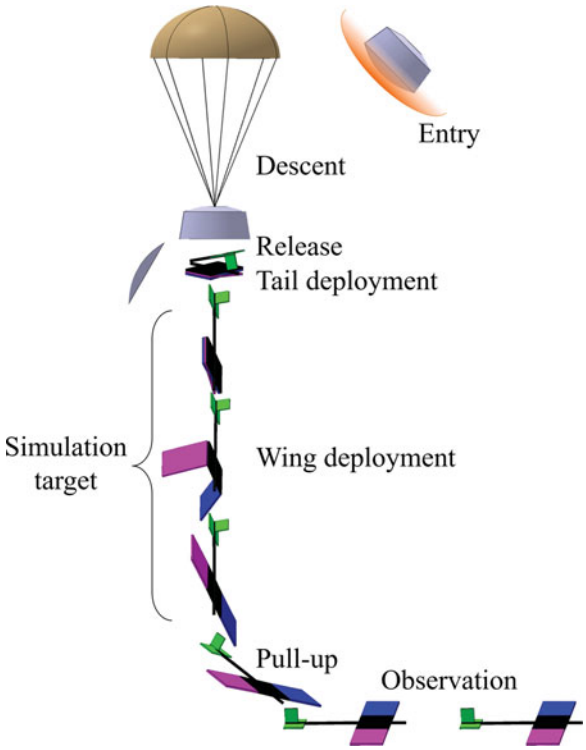

Figure 1. (Colour online) Mission scenario and simulation target.

behaviour from nominal and may present a risk of failure. The aerial deployment process cannot afford to fail. Therefore, a consideration of the robustness of the aerial deployment is important for the Mars aircraft.

Fujita et al have investigated the aerial deployment of the Mars aircraft with folding wings with the help of a multibody dynamics simulation[7-10]. Their work includes the derivation of the equations of motion of the multibody system, the motion analyses of the symmetric and asymmetric wing deployments at nominal conditions, and the sensitivity analysis. As mentioned above, the previous research focused on the establishment of the simulation method and the understanding of the aerial deployment motion itself. In the next step, we must perform a design exploration of the deployment mechanism considering the robustness under variations of the deployment conditions. This study presents a design of a deployment mechanism that is able to perform safe aerial deployment while maintaining a low torque for deployment and remaining lightweight under various conditions. In particular, this study investigates the effect of the deployment mechanism torque and the deployment timing on the deployment behaviour.

2.0 MISSION SCENARIO AND SIMULATION TARGET

Figure 1 shows a mission scenario and the simulation target. The Mars aircraft will be transported to Mars packed in an entry capsule. At Mars, the entry capsule will enter and descend into the Martian atmosphere with a parachute. When the entry capsule arrives at a

https://doi.org/10.1017/aer.2016.123 Published online by Cambridge University Press

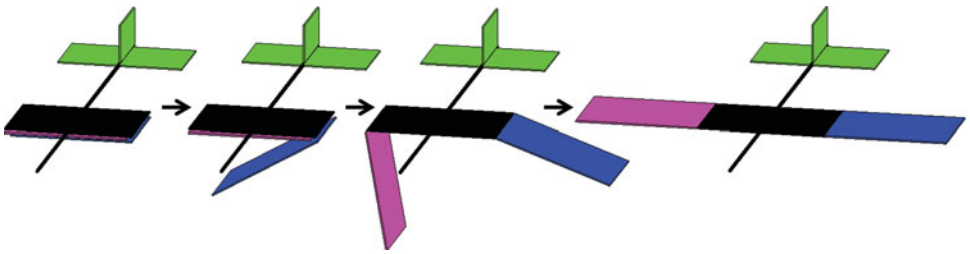

Figure 2. (Colour online) Wing deployment process.

predefined position, the Mars aircraft will be released from the entry capsule and will perform aerial deployment. The tail will be deployed first, and then the main wings will be deployed. The fully deployed Mars aircraft will control its attitude and start a horizontal flight. The Mars aircraft is able to conduct observations such as Martian magnetic field observations, thus capturing vast areas of the surface.

Manoeuvres after the deployment, i.e. pull-up and observation flight, can be analysed using a usual flight simulation method that treats the aircraft as a single rigid body. However, the deployment process cannot be analysed using this method. The analysis of the deployment process requires a multibody dynamics simulation method. A motion analysis of the deployment process is important because the final condition of the deployment process coincides with the initial condition of the pull-up and observation flight. In addition, this study is focused on the design of the deployment mechanism of the main wing. Therefore, the simulation was performed from the end of the tail deployment to the end of the main wing deployment.

In the past, design of the deployment mechanism for a folding wing was carried out through a trial-and-error process. Therefore, the effect of the design on the deployment motion has not been clarified quantitatively. The simulation in this paper reveals how the design variables physically and quantitatively affect the aerial deployment behaviour.

3.0 SIMULATION METHOD

Although the Mars aircraft deploys not only the main wing but also the tail, this study deals with the deployment of the main wing. The analysis model consisted of three rigid bodies: a centre body, a right wing and a left wing. These bodies will be referred to as rigid bodies A, B and C in this paper. The centre body consisted of a centre wing, a fuselage and a tail. The right and left wings were assumed to be flat plates. Each body was connected to each other with spring-loaded hinges.

Figure 2 shows a wing deployment process. At first, the right and left wings were folded under the fuselage. Then both wings rotated around the hinges. The rotation stopped when the wings aligned with the centre wing. In this study, the left wing always started its deployment at the beginning of the simulation. However, to avoid contact between the wings, the right wing did not start its deployment simultaneously; the right wing started its deployment after the deployment delay time T_{SR}. The hinge axis was set along the chord direction because this configuration allows for the wings to be placed in parallel when in the folded state.

This study used the aerial deployment motion simulator in Ref. 7. As described above, the model was a multibody system consisting of the three rigid bodies connected with hinges.

https://doi.org/10.1017/aer.2016.123 Published online by Cambridge University Press

The equations of motion for this multibody system were reported in Ref. 8. The equation of motion of the folding wing aircraft was derived using a velocity transformation method[11]. External forces were the aerodynamic force, the hinge torque and gravity. Therefore, the motion was affected by the aerodynamic force. However, the aerodynamic force is a function of the velocity relative to the air. Hence, the aerodynamic force was also affected by the motion.

From an aerodynamics perspective, the aerial deployment process is a complex problem. The points to consider include the low Reynolds number flow ($Re = O(10^4)$), the flow separation, the process time (several seconds), the three-dimensional body and flow, and the wing motion. A potential-flow-based method and a method based on the Reynolds-averaged Navier-Stokes equations (RANS) method usually cannot treat the separated flow. On the other hand, although the large eddy simulation (LES) and the direct numerical simulation (DNS) can treat the separation, they cannot calculate the flow around the three-dimensional aircraft with wings in motion for such a long period of time.

Therefore, this study applied the experimental results of the aerodynamic characteristics of a flat plate to the wings and the tails as basic characteristics. The total aerodynamic characteristics (i.e. data from all 360° of angles-of-attack) of the flat plate were obtained by Okamoto et al[12] and were used for the longitudinal characteristics. The effect of a sideslip was evaluated based on Ref. 13. It should be noted that the interaction of the flows around the bodies was ignored. Therefore, the aerodynamic characteristics were independent of the deployment angle. Although the deployment angle was independent, the deployment speed affected the aerodynamic force through the change of the air speed, angle-of-attack and sideslip angle.

The dynamic derivatives were not introduced for each flat plate. However, some of the derivatives were approximately introduced as a nature of this multibody dynamics. The aerodynamic force of each flat plate was independently calculated using the local air velocity vector at a reference point of each plate. On the other hand, one of the typical estimation methods for the dynamic derivatives of the aircraft calculates the dynamic derivatives based on the local difference of the aerodynamic force due to local air velocity vector using the strip theory[14]. Therefore, the effect of such dynamic derivatives was automatically and approximately reflected in the simulation. The derivatives produced by the difference of the forces between the right and the left wing due to its rotation (i.e. C_{lp}, C_{lr}, C_{np} and C_{nr}), and the derivatives produced by the change of the forces acting on the tail due to its rotation (i.e. C_{mq}, C_{lr}, C_{nr} and C_{Yr}), were approximately effective. It should be noted that the design dihedral in this simulation is zero. However, if the dihedral exists, additional derivatives such as $C_{l\beta}$, etc. are also approximately effective.

In summary, this model can simulate a post-stall condition fast enough using the experimental result of the aerodynamic characteristics. Some of the dynamic derivatives were approximately introduced as a nature of this multibody dynamics. This model can also simulate the three-dimensional behaviour of the aircraft with moving wings.

A drive power was affected on the hinges as a torque owing to the deployment mechanism. Owing to the characteristics of the spring, the strength of a spring was at its weakest when the wing was in the deployed state. The torque of the spring while the wings are in the deployed state $T_{\text{spring}|\text{Dep}}$ shall be used as the standard in this simulation. In order to design an appropriate strength of the spring under a variety of deployment conditions, it was considered appropriate to relate the strength of the spring with a torque owing to the aerodynamic forces. A deployment torque scale F was, therefore, defined in this study as a dimensionless quantity expressed by the ratio of the torque due to the deployment mechanism T_{deploy} to the torque due

https://doi.org/10.1017/aer.2016.123 Published online by Cambridge University Press

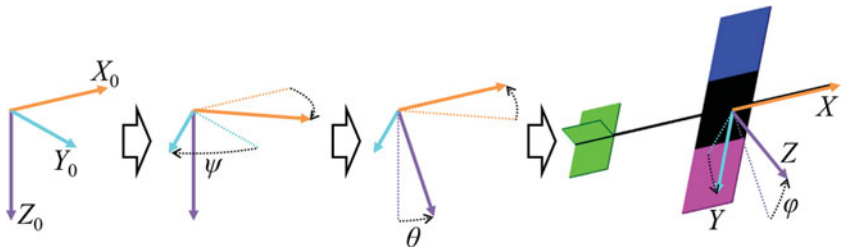

Figure 3. (Colour online) Definition of the Euler angle.

to the aerodynamic forces T_{aero}

$$F \equiv \frac{T_{\text{deploy}}}{T_{\text{aero}}} = \frac{T_{\text{spring}}\big|_{\text{Dep}}}{T_{\text{aero}}} = \frac{2\,T_{\text{spring}}\big|_{\text{Dep}}}{l{b_{\text{out}}}^2} = \frac{2\,T_{\text{spring}}\big|_{\text{Dep}}}{qcC_{L,\,W,\,\max}{b_{\text{out}}}^2} = \frac{2\,T_{\text{spring}}\big|_{\text{Dep}}}{qS_{\text{out}}b_{\text{out}}C_{L,\,W,\,\max}}, \quad \ldots (1)$$

where S_{out} and b_{out} are the wing area and span of the outer wing respectively, l is a maximum lift force per unit wing span, c is a chord length and q is a dynamic pressure. The maximum lift coefficient of the main wing $C_{L,W,\max}$ was assumed to be 1 based on the aerodynamic characteristics of the flat plate[12]. The deployment mechanism torque was obtained as a function of the deployment torque scale F. In this study, the deployment mechanism torque was treated as a value that was independent of the deployment angle to reduce the parameter because a change in the deployment mechanism torque due to deployment angle was not essential.

Atmospheric density and gravitational acceleration can be expressed as a function of altitude. The atmospheric density on Mars was calculated based on Ref. 15. The gravitational acceleration was calculated using the law of gravity. The incident angle of the main wing was 0°. The incident angle of the horizontal tail was set to 5° to make the trim angle-of-attack positive. Here, the positive direction of the incident angle of the horizontal tail is the direction in which the leading edge of the horizontal tail aimed downward. The trim angle-of-attack was 8.8° and the true airspeed at the equilibrium gliding condition was 65 m/s. The quaternion was used for the attitude expression in this simulation and the Euler angle was used only for the output. Figure 3 shows a definition of the Euler angle. It should be noted that, in this study, the downward direction was set to the direction to which all Euler angles were zero. It means that the X_0, Y_0 and Z_0 directed to the ground, the east and the south, respectively. The reason why the reference of the Euler angle changed is that the initial condition of this simulation was mainly the downward dropping condition as it will be later described; this attitude was a singular attitude for the usual Euler angle definition. An Adams-Bashforth-Moulton PECE solver was used as the numerical integration method[16].

4.0 ROBUSTNESS EVALUATION

A sigma level method[17,18] was adopted for the robustness evaluation. The sigma level is a function of the average and the standard deviation of the evaluation function. The average and the standard deviation were calculated using the sensitivity method. The sensitivity was numerically obtained using some of the results from the simulations. Evaluation functions in this study were margins for safe deployment conditions, which were defined in this section.

https://doi.org/10.1017/aer.2016.123 Published online by Cambridge University Press

Table 1
Relation between the sigma level and its safety probability[18]

Sigma level n	Safety probability (%)
1	68.25
2	95.46
3	99.73
4	99.9937
5	99.999943
6	99.9999998

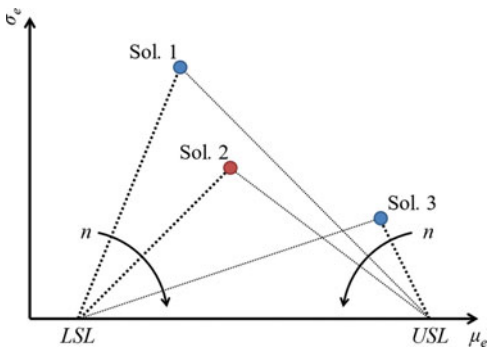

Figure 4. (Colour online) Concept of the sigma level n.

A sigma level method is one of the suitable ways to evaluate the robustness for the problem, which has constraints for the evaluation function. The sigma level n indicates the probability of the evaluation function staying within the constraints. The sigma level n was defined as follows:

$$n \equiv \min\left(\frac{\mu_e - LSL}{\sigma_e}, \quad \frac{USL - \mu_e}{\sigma_e}\right), \qquad \ldots(2)$$

where LSL and USL are the lower and upper specification limits respectively, and μ_e and σ_e are the average and the standard deviation of the evaluation function e, respectively. A concept of the sigma level is shown in Fig. 4. The sigma level n is a measure of the distance between the average and the specification limits based on the standard deviation. Therefore, the sigma level n can be graphically understood as an inverse of the slope of the line connecting the lower/upper specification limits with the result of the average and the standard deviation of the evaluation function. For example, the solution of the lowest standard deviation is Sol. 3. However, because the average of Sol. 3 is close to the specification limit, the possibility of failure is not the lowest, and therefore the sigma level is not the highest. Solution 1 is worse than Sol. 2 because the average is closer to the limit, and the standard deviation is larger. The solution of the highest sigma level, and therefore of the highest robustness, is Sol. 2, owing to the balance of the average and the standard deviation. As described above, usage of the sigma level is effective to evaluate the robustness of the evaluation function, which has constraints. Table 1 shows the relation between the sigma level n and its safety probability[18].

https://doi.org/10.1017/aer.2016.123 Published online by Cambridge University Press

The sigma level method uses the average and the standard deviation of the evaluation function caused by the variation of the dispersive input variables. There are two calculation methods of the average and the standard deviation: the sensitivity method and the Monte Carlo method[19]. The sensitivity method numerically calculates the sensitivity to the evaluation function, and obtains the average and the standard deviation of the evaluation function using the Taylor expansion. The Monte Carlo method collected the result of the simulation by randomly changing the dispersive input variables, and then the average and the standard deviation were calculated based on the obtained data set. The sensitivity method is better from the standpoint of the balance of accuracy and calculation cost when the number of the dispersive input variables is low. Since the number of dispersive input variables for this study was low, as will be described later, the sensitivity method was adopted.

The j-th evaluation function $e_j(\mathbf{x})$ of the dispersive input variables vector $\mathbf{x}$ can be written using the Taylor expansion, as follows:

$$e_j(\mathbf{x}+\Delta\mathbf{x}) = e_j(\mathbf{x}) + \left(\frac{\partial e_j}{\partial \mathbf{x}}\right)^T \Delta\mathbf{x} + \frac{1}{2}\Delta\mathbf{x}^T \frac{\partial^2 e_j}{\partial \mathbf{x}^2}\Delta\mathbf{x} + O(\Delta\mathbf{x}^3). \quad \ldots(3)$$

The average and the standard deviation of the evaluation function μ_{ej} and $\sigma_{ej,i}$ respectively, can be obtained using Equation (3). On collecting the terms up to the first order, we obtain:

$$\mu_{e_j} = e_j(\mu_{\mathbf{x}}), \quad \ldots(4)$$

$$\sigma_{e_{j,i}} = \sqrt{\left(\frac{\partial e_j}{\partial x_i}\right)^2 {\sigma_{x_i}}^2}, \quad \ldots(5)$$

where $\boldsymbol{\mu}_{\mathbf{x}}$ is the average vector of the dispersive input variables and σ_{xi} is the standard deviation of the i-th dispersive input variable x_i. Both $\boldsymbol{\mu}_{\mathbf{x}}$ and σ_{xi} are defined by the user. The first-order approximation was used to reduce the calculation cost.

The sensitivity of the dispersive input variables to the evaluation function was numerically obtained. It is expressed using the difference method as follows:

$$\frac{\partial e_j}{\partial x_i} \approx \frac{e_j(\mathbf{x})\big|_{x_i=\mu_{x_i}+\Delta x_i} - e_j(\mathbf{x})\big|_{x_i=\mu_{x_i}}}{\Delta x_i}, \quad \ldots(6)$$

where μ_{xi} is the average of the i-th dispersive input variable x_i and Δx_i is a difference of x_i for the sensitivity calculation.

In this study, the sigma level n was a function of the design variables, evaluation functions and dispersive input variables. Therefore, it was calculated for each design point, evaluation function and dispersive input variable.

$$n = f(\text{Design variables},\ ID_{\text{Eval}},\ ID_{\text{Disp}}), \quad \ldots(7)$$

where ID_{Eval} and ID_{Disp} are the identification number of the target evaluation function and dispersive input variable, respectively.

https://doi.org/10.1017/aer.2016.123 Published online by Cambridge University Press

In this paper, a minimum sigma level $n_{\min}$ was defined as the minimum value of the sigma level of all evaluation functions for each design point and each dispersive input variable. Thus, the minimum sigma level $n_{\min}$ was a function of the design variables and the dispersive input variables. Here, evaluation functions contributing to the minimum sigma level $E^*_{\text{contributing}}$ can be obtained as a function of the design variables and the dispersive input variables.

$$n_{\min} = f(\text{Design variables},\ ID_{\text{Disp}}). \quad \ldots(8)$$

$$E^*_{\text{contributing}} = f(\text{Design variables},\ ID_{\text{Disp}}). \quad \ldots(9)$$

Furthermore, a total minimum sigma level $n_{\min\ \text{Total}}$ was defined as a minimum value of the sigma level of all evaluation functions and all dispersive input variables for each design point. Thus, the total minimum sigma level $n_{\min\ \text{Total}}$ was a function of only the design variables. Here the evaluation functions and the dispersive input variables contributing to the total minimum sigma level, $E_{\text{contributing}}$ and $V_{\text{contributing}}$, can be obtained as a function of only the design variables.

$$n_{\min\ \text{Total}} = f(\text{Design variables}). \quad \ldots(10)$$

$$E_{\text{contributing}} = f(\text{Design variables}). \quad \ldots(11)$$

$$V_{\text{contributing}} = f(\text{Design variables}). \quad \ldots(12)$$

5.0 SIMULATION CONDITION

5.1 Design variables

Since fundamental specifications (e.g. planform of the aircraft) were designed depending on the total performance of the aircraft, such variables were constant in the analysis of the robustness. The design variables for this robustness analysis were the variables that were directly related to the aerial deployment: the deployment torque scale F and the right-wing deployment delay time T_{SR}. The deployment torque scale F has been defined by Equation (1), and it represents the ratio of torques between the deployment mechanism and the aerodynamic force. The range of the deployment torque scale F was set from 0 to 1.5. On the other hand, the right-wing deployment delay time T_{SR} is the time difference between the starting time of the deployment of the right and the left wing. The range of the right-wing deployment delay time T_{SR} was set from 0 to 2 s. It should be noted that the left wing always started its deployment at the beginning of the simulation. There were 21 design points for each design variable at regular intervals. The total number of the design points was $21 \times 21 = 441$.

5.2 Evaluation functions

In this study, the evaluation functions were margins for the safe deployment conditions. The safe deployment conditions are shown in Table 2. Three requirements were set as the safe deployment conditions to determine either the success or the danger of the aerial deployment motion. The margin was defined as follows:

$$\text{Margin} = \min\ (\min(\text{Value}) - \text{Lower limit},\ \text{Higher limit} - \max(\text{Value})) \quad \ldots(13)$$

https://doi.org/10.1017/aer.2016.123 Published online by Cambridge University Press

Table 2
Safe deployment condition for analysis of robustness

	Limitation			
Name	**Low**	∼	**High**	**Unit**
Load factor	–3	∼	5	–
Hinge reaction moment	–	∼	18	N· m
Main wing bending	–16	∼	26	N· m

Value is a time-series data of the target parameter. A minimum or a maximum value in the simulation was used. The margin must be positive. The higher the margin is, the safer the deployment. Therefore, *LSL* and *USL* for the margin were 0 and nothing, respectively. Meanwhile, the failure of the aerial deployment motion was defined as the wings not having been fully deployed at the end of the simulation, or the right wing tip contacting the left wing.

The limit load factor requirements n_{limit} were set to 5 and –3. The upper requirement was designed higher than conventional ones[20]. Since the angle-of-attack of the deploying aircraft took on not only positive but also negative values, the lower limit of the load factor was also important. Therefore, the lower limit of the load factor was set to –3 to withstand the aerodynamic force at a negative angle-of-attack.

A hinge reaction moment was regulated to prevent the structure near the hinge from breaking. The strength of the structure was expressed based on a limit load factor n_{limit}. The required hinge reaction moment $M_{\text{Reac Req}}$ was written as the following equation:

$$M_{\text{Reac Req}} = \frac{n_{\text{limit}} m_{\text{total}} g b_{\text{out}}^2}{2b}, \quad \ldots (14)$$

where m_{total}, g, and b represent the total mass, acceleration due to gravity and span, respectively. It was assumed that the span of each rigid body was the same; therefore $b_{\text{out}} = b/3$. The sign of the moment was positive for the right hinge and negative for the left hinge. Reference 7 revealed that the most sensitive condition was the hinge reaction moment. Therefore, the structure was reinforced and the limitation of the hinge reaction moment was changed to the value based on a load factor of 8. Here, the additional mass of the reinforcement was ignored.

The main wing may be damaged by the bending moment caused by the deployment of the right and left wings. Therefore, the bending moment at the centre of the main wing span $M_{b/2}$ due to the Z-direction force on the centre wing $F_{Z\text{Aw}}$ and the hinge moment M_{hinge} was determined using Equation (15).

$$\begin{aligned} &\text{for } M_{\text{hinge},B} \cdot M_{\text{hinge},C} < 0 \\ &\quad M_{b/2} = \frac{F_{ZAw} b_A}{8} + \text{sgn}\left(M_{\text{hinge},B}\right) \min\left(\left|M_{\text{hinge},B}\right|, \left|M_{\text{hinge},C}\right|\right), \\ &\text{for } M_{\text{hinge},B} \cdot M_{\text{hinge},C} \geq 0 \\ &\quad M_{b/2} = \frac{F_{ZAw} b_A}{8}, \end{aligned} \quad \ldots (15)$$

https://doi.org/10.1017/aer.2016.123 Published online by Cambridge University Press

Table 3
Specifications of rigid bodies

Name		Body A	Body B, C	Unit
Mass		4.3	0.16	kg
Wing area		0.41	0.41	m^2
Chord		0.51	0.51	m
Span		0.80	0.80	m
CG	X_{CG}	0.2	0.2	m
	Y_{CG}	0	±0.80	m
	Z_{CG}	0	0	m
Inertia matrix	I_{XX}	0.20	0.0087	kg· m^2
	I_{YY}	1.1	0.0039	kg· m^2
	I_{ZZ}	1.2	0.012	kg· m^2
	I_{XZ}	−0.088	0	kg· m^2

#The origin of the coordinates for CG position expression was the point on the leading edge, the upper surface, the centre in spanwise of the main wing.

where b_A is the span of the centre wing. The first term represents the bending moment due to the aerodynamic force. Here, a uniformly distributed aerodynamic force was assumed. The second term represents the bending moment due to the hinge moments. The bending moment varies depending on the combination of the moments on the right and left hinges. When the directions of the hinge moments are the same, the bending moment due to hinge is zero, and the body rotates according to the sum of the moments. On the other hand, when the directions of the hinge moments are opposite, a bending moment due to the hinge occurs, and the body rotates according to the difference of the moments. The magnitude of this bending moment due to the hinge moments is equal to the lowest hinge moment. Here, the limitation was set as a bending moment at a limit load factor n_{limit}.

5.3 Nominal condition

The specifications of the rigid bodies are shown in Table 3. The specifications were defined based on those of the Mars aircraft[21]. The masses of the right and left wings were both set to 0.16 kg. The mass of the centre was obtained as the difference between the mass of the Mars aircraft and the sum of the right and left wings. Inertia matrices of the right and left wings are calculated as a 0.050 m thick and uniform-density flat plate. The X-coordinate of the reference point of the inertia calculation was set to the centre of gravity of the whole aircraft. The Y and Z coordinates of the reference point were set to the centre of the flat plate. Since there are plane symmetries with respect to the XY plane and the XZ plane, the product of inertia of the right and left wings around the reference point was zero. An inertia matrix of the centre body was calculated from the values of the Mars aircraft and the right and left wings using the parallel axis theorem.

Table 4 shows the nominal conditions. g and T_{SL} are the acceleration due to gravity and left wing deployment delay time, respectively; h is the height; U_A, V_A and W_A are the translational velocities; φ_A, θ_A and ψ_A are the attitude angles; P_A, Q_A and R_A are the angular rates; and θ_{dep} and $(d\theta_{dep}/dt)$ are the deployment angle and its speed. This condition means that the wing-folded aircraft drops aiming its nose downwards with a velocity of 65 m/s. Therefore, the initial flight-path angle was –90°. The left wing started its deployment when the simulation

https://doi.org/10.1017/aer.2016.123 Published online by Cambridge University Press

Table 4
Nominal conditions

	Variable	Nominal	Unit
Constants	g	3.7	m/s^2
	T_{SL}	0	s
Initial values	h_0	8000	m
	$U_{A\,0}$	65	m/s
	$V_{A\,0}$, $W_{A\,0}$	0	m/s
	$\theta_{A\,0}$	0	deg
	$\varphi_{A\,0}$, $\psi_{A\,0}$	0	deg
	$P_{A\,0}$, $Q_{A\,0}$, $R_{A\,0}$	0	deg/s
	$\theta_{dep\ 0}$	0	deg
	$(d\theta_{dep}/dt)_0$	0	deg/s

began. The right wing started its deployment after the right-wing deployment delay time T_{SR} had passed. The simulation time was limited to the value of the right-wing deployment delay time T_{SR} plus 2 s. This limitation is useful for the reduction of the total calculation cost. The control surfaces were fixed to check the effect of the input conditions on the behaviour.

5.4 Dispersive input variables

A scope of the variation was defined considering the aerial deployment condition on Mars. The important dispersive input variables are as follows:

- Initial drop velocity
- Surrounding gust velocity
- Initial pitch angle
- Initial height

First, let us focus on the initial drop velocity. The current mission has a deceleration phase using a parachute before the deployment. Therefore, the initial drop velocity can be estimated from the terminal velocity of the parachuting condition. The terminal velocity V_{terminal} can be obtained from the balance of the gravity and drag.

$$V_{\text{terminal}} = \sqrt{\frac{2m_{\text{total}}g}{\rho S_{\text{parachute}} C_{D\,\text{parachute}}}}, \qquad \ldots (16)$$

where ρ, $S_{\text{parachute}}$, and $C_{\text{Dparachute}}$ are the atmospheric density and the reference area and the drag coefficient of the parachute, respectively. Since the average of the terminal velocity can be designed through the parachute, the value was set to 65 m/s based on the cruising velocity. The standard deviation was considered next. In Equation (16), the density and the drag coefficient can vary from the nominal condition. In this study, the standard deviation of the initial drop velocity was assumed to be 10% of the average velocity.

The surrounding gust in the vertical direction was then ignored because it was almost the same as the variation of the drop velocity. Therefore, only the surrounding gust in

https://doi.org/10.1017/aer.2016.123 Published online by Cambridge University Press

the horizontal direction was considered. Based on Ref. 6, the average and the standard deviation of the surrounding gust velocity were defined as 30 m/s and 20% of the average, respectively. The direction of the surrounding gust in relation to the aircraft was unpredictable. In this study, the direction of the surrounding gust was set to the direction from the right-wing side to the left-wing side in the initial condition because the direction showed worst result.

A third dispersive input variable is the initial pitch angle. An initial flight-path angle was fixed to –90°, i.e. dropping condition. Here, we considered the situation that the initial pitch angle varies while keeping the flight-path angle. Therefore, the initial angle-of-attack of the centre body was the same as the initial pitch angle. The average of the pitch angle at the beginning of the deployment varies depending on the trim angle in the folded state, the condition of the control surfaces, etc. The standard deviation of the pitch angle varies depending on the surrounding wind, the unsteady aerodynamic force for folded-state aircraft, the attitude control using control surfaces, the natural frequency of the aircraft pitching motion, etc. Therefore, the average and the standard deviation of the initial pitch angle were assumed to be 0° and 10°, respectively. It should be noted that an attitude with the aircraft nose aiming toward the ground and the upper surface aiming toward the north had been set to the origin of the Euler angle of attitude to avoid the singularity.

The final dispersive input variable is the initial height. The change of the height has an impact on the atmospheric density. The average initial height was set to 8 km using the ARES[2] as reference. The standard deviation of the initial height was defined to be 20% of the average. The atmospheric density at the height of 8 km is approximately 0.008 kg/m^3.

6.0 RESULTS AND DISCUSSION

The sigma levels of the margins for the safe deployment conditions for each variation of the aerial deployment condition are discussed first. After that, the optimal value, the successful region and the contributing factors of the total minimum sigma level are evaluated.

Figure 5 shows the sigma levels for the variation of the initial drop velocity. The legend "Success" means both wings were fully deployed and all safe deployment conditions were satisfied. The legend "Danger" means both wings were fully deployed, but at least one of the safe deployment conditions was violated. The legend "Failure" means that the right or left wing was not fully deployed or the right wing tip hit the left wing. The sigma level of the load factor showed relatively low values from $(F, T_{SR}) = (0.5, 0.3)$ to $(F, T_{SR}) = (1.5, 0.7)$, and from $(F, T_{SR}) = (0.8, 1.5)$ to $(F, T_{SR}) = (1.5, 1.8)$. This might be caused by the balance between the period of the motion and the right wing deployment delay time T_{SR}. The minimum sigma level n_{min} of more than 5 was obtained at large region of the design space.

Figure 6 shows the sigma levels for the variation of the surrounding gust. The sigma level of the hinge reaction moment was lower than that of the initial drop velocity. This suggests that the wing deploys too rapidly owing to the surrounding gust. A high sigma level can be achieved at the design space where the deployment torque scale F is below 0.8, and the right-wing deployment delay time T_{SR} is from 0.2 to 1.2 s. Figure 5 indicates that the contributing factor for the minimum sigma level n_{min} for the variation of the surrounding gust is the hinge reaction moment.

https://doi.org/10.1017/aer.2016.123 Published online by Cambridge University Press

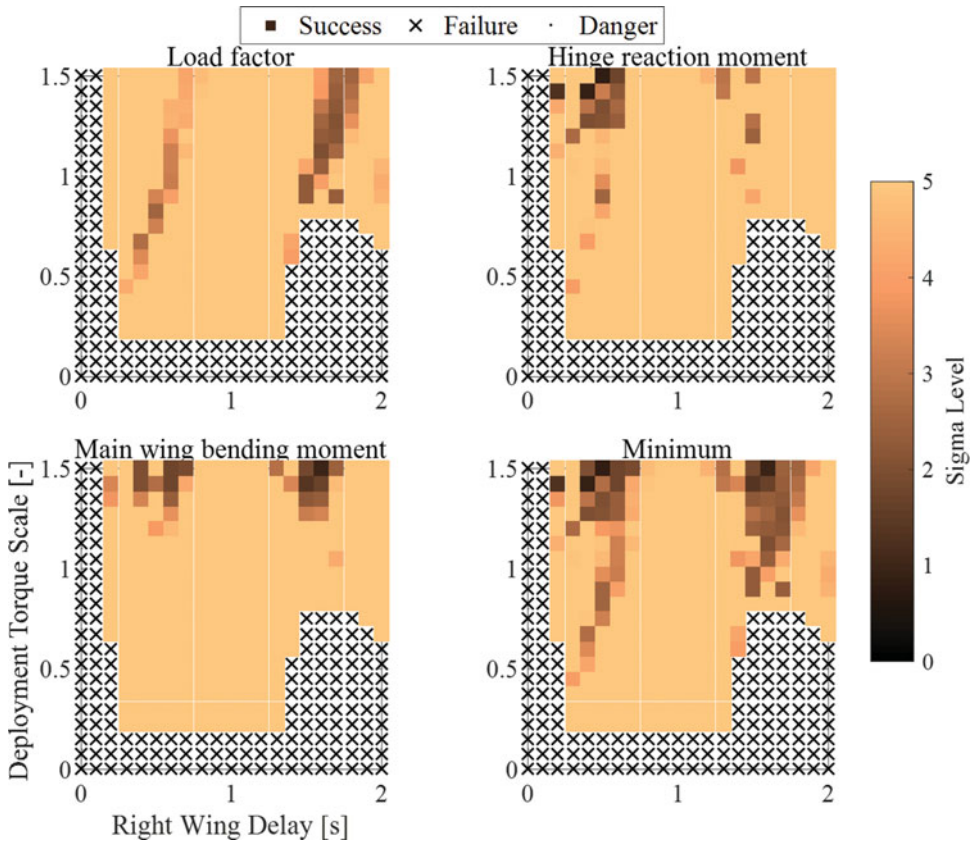

Figure 5. (Colour online) Sigma levels for variation of initial drop velocity.

Figure 7 shows the sigma levels for the variation of the initial pitch angle. The sigma level of the limit load factor is lower than that of the variations of the initial drop velocity and the surrounding gust. This reduction is caused by the change of the extremal value of the angle-of-attack due to the initial pitch angle change. The important result is that the lower limit of the successful deployment torque scale F increased to 0.5. This increase is the effect of the folding-direction aerodynamic force due to a bad initial pitch angle.

Figure 8 shows the sigma levels for the variation of the initial height. Overall, the effect of the initial height is lower than other variations, and each sigma level has a relatively high value.

Figure 9 shows the total minimum sigma level $n_{\min\ \mathrm{Total}}$, which is the minimum value among the minimum sigma level $n_{\min}$ of each variation. In addition, $V_{\mathrm{contributing}}$ and $E_{\mathrm{contributing}}$, the dispersive input variables and the safe deployment conditions contributing to the total minimum sigma level $n_{min\ Total}$, are shown in Figs. 10 and 11, respectively. Globally, there are high sigma level regions at the deployment torque scale below 0.8, and the right-wing deployment delay time T_{SR} from 0.4 to 1.3 s. The result indicates that a low deployment-torque-scale F yields a high sigma level. However, the minimum value of the successful deployment torque scale F was approximately 0.5. This limitation depends on the aerial deployment performance in the variation of the initial pitch angle, as shown in Fig. 6. The

https://doi.org/10.1017/aer.2016.123 Published online by Cambridge University Press

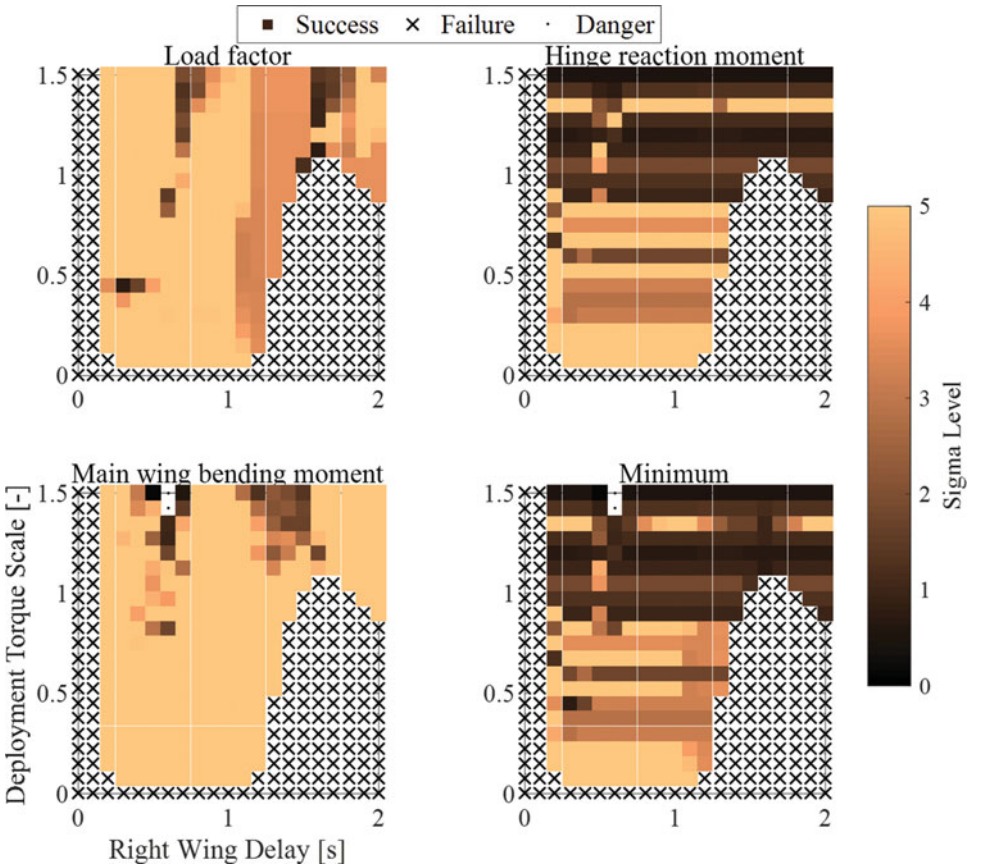

Figure 6. (Colour online) Sigma levels for variation of surrounding gust.

change of the initial pitch angle caused a change in the angle-of-attack, which caused difficulties in the deployment of the wing. Therefore, the wings could not be deployed in the low deployment-torque design. In Fig. 9, the dispersive input variables contributing to the total minimum sigma level $V_{\text{contributing}}$, indicate that the variation of the surrounding gust has a high impact in general. On the other hand, in Fig. 10, the safe deployment conditions contributing to the total minimum sigma level $E_{\text{contributing}}$, indicate that the load factor and the hinge reaction moment have a high impact. As seen in the comparison of Fig. 9 to Fig. 10, the contributing factors at the high-sigma-level region are the condition of the load factor due to the initial pitch angle, and the safe deployment condition of the hinge reaction moment due to the surrounding gust. The results described above quantitatively clarified the effect of the deployment torque scale F and the right-wing deployment delay time T_{SR} on the robustness of the safe aerial deployment under a variety of conditions.

The design point of the deployment torque scale F is 0.7, and the right-wing deployment delay time T_{SR} of 1.0 s was selected as a low deployment-torque-scale F and high sigma level n design. The total minimum sigma level $n_{\text{min Total}}$ of this design point is more than 5. The sigma level around the design point is also relatively high. In addition, the selected design point has a margin of the deployment torque scale F of 0.1 to the failure condition of 0.5. The

https://doi.org/10.1017/aer.2016.123 Published online by Cambridge University Press

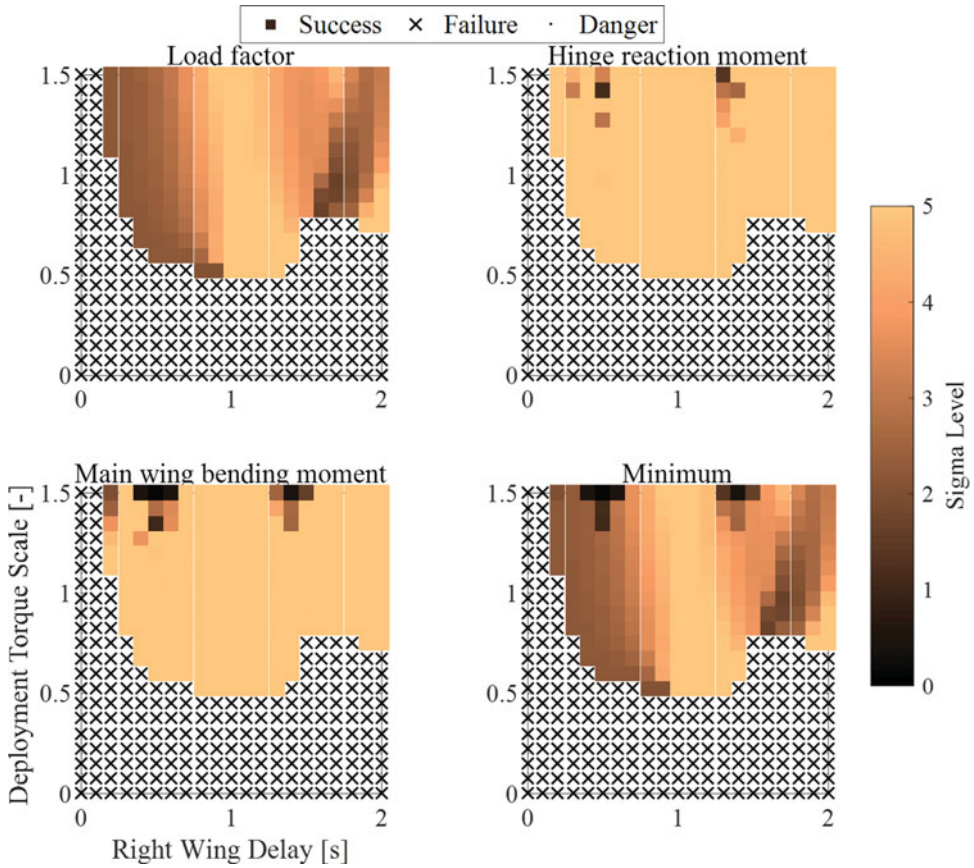

Figure 7. (Colour online) Sigma levels for variation of initial pitch angle.

selected design point is expected to deploy safely and surely while keeping a low deployment-torque-scale F.

7.0 CONCLUSIONS

The robustness of aerial deployment behaviour was investigated in this study. The deployment torque scale F was defined as an effective design variable for wing deployment in the variable aerodynamic condition. The design variables were the deployment torque scale F and the right-wing deployment delay time T_{SR}. The evaluation functions were the sigma levels of the margins for the safe deployment conditions. The dispersive input variables were the initial drop velocity, the surrounding gust speed, the initial pitch angle and the initial height. The result showed that the design point with a deployment torque scale F of 0.7 and a right-wing deployment delay time T_{SR} of 1.0 s was able to deploy safely in the low-torque deployment condition. This point is able to accomplish both safe deployment and light weight of the deployment mechanism. The lower limit of the deployment torque scale F was restricted by the variation of the initial pitch angle. The change of the initial pitch angle caused a change in the angle-of-attack of the right and left wings, and prevented them from deploying in the

https://doi.org/10.1017/aer.2016.123 Published online by Cambridge University Press

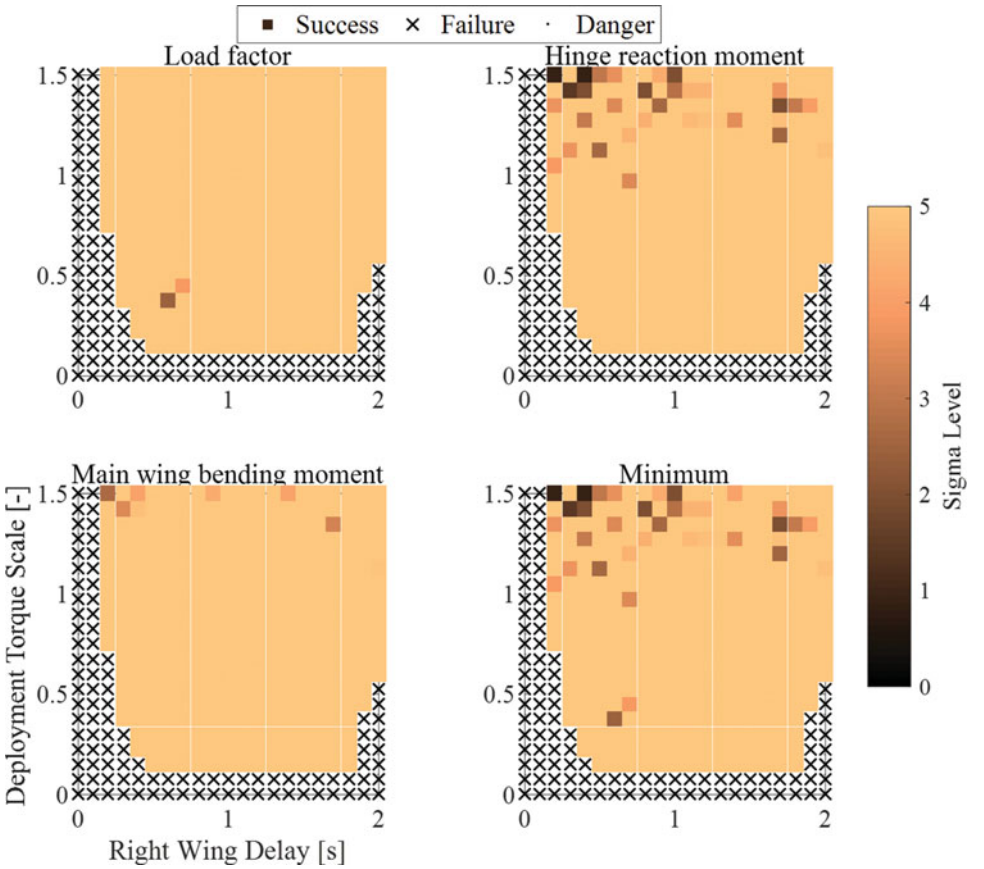

Figure 8. (Colour online) Sigma levels for variation of initial height.

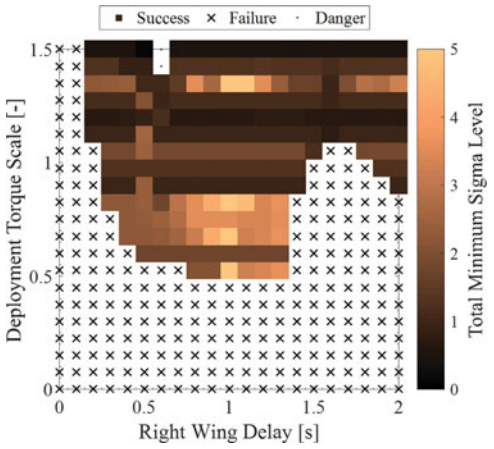

Figure 9. (Colour online) Total minimum sigma level $n_{\text{min Total}}$.

https://doi.org/10.1017/aer.2016.123 Published online by Cambridge University Press

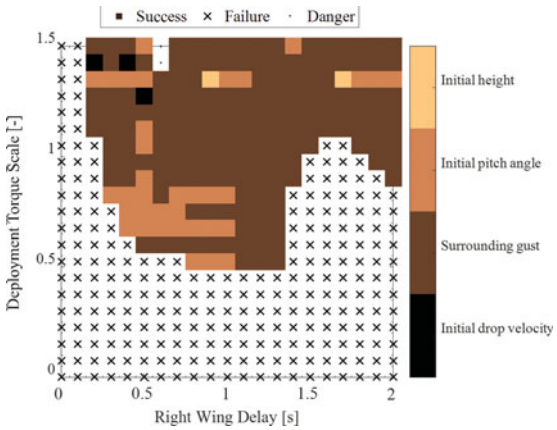

Figure 10. (Colour online) Dispersive input variables contributing to the total minimum sigma level $V_{\text{contributing}}$.

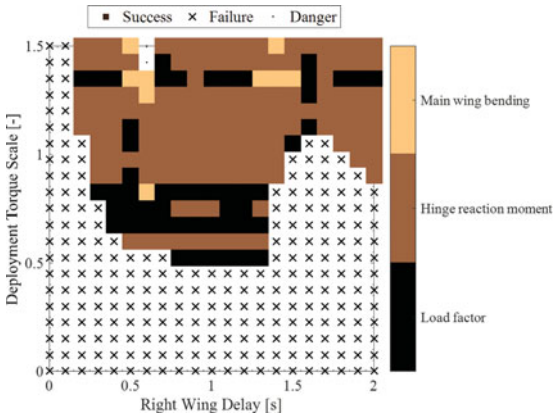

Figure 11. (Colour online) Safe deployment conditions contributing to the total minimum sigma level $E_{\text{contributing}}$.

low deployment-torque design. Bottleneck factors in the high-sigma-level region were the safe deployment condition of the load factor under the initial pitch angle dispersion, and the safe deployment condition of the hinge reaction moment under the surrounding gust dispersion.

ACKNOWLEDGEMENTS

This work was partially supported by the Mars Exploration Airplane Working Group of the Institute of Space and Astronautical Science, Japan Aerospace Exploration Agency, and by a Grant-in-Aid for Scientific Research (A), No. 24246136.

https://doi.org/10.1017/aer.2016.123 Published online by Cambridge University Press

REFERENCES

1. JACOB, J.D. and SMITH, S.W. Design limitations of deployable wings for small low altitude UAVs, Proceedings of the 47th AIAA Aerospace Sciences Meeting Including The New Horizons Forum and Aerospace Exposition, AIAA 2009-1291, January 2009, Orlando, Florida, US.
2. GUYNN, M.D., CROOM, M.A., SMITH, S.C., PARKS, R.W. and GELHAUSEN, P. A. Evolution of a Mars airplane concept for the ARES Mars Scout Mission, Proceedings of the 2nd AIAA Unmanned Unlimited Systems, Technologies, and Operations, AIAA 2003-6578, September 2003, San Diego, California, US.
3. HALL, D.W., PARKS, R.W. and MORRIS, S. Airplane for Mars exploration, NASA TR, 1997, NASA Ames Research Center, Moffett Federal Airfield, California, US.
4. BOVAIS, C. S. and DAVIDSON, P. T. Flight testing the flying radar target (FLYRT), Proceedings of the 7th Biennial Flight Test Conference, AIAA-94-2144-CP, 279-286, June 1994, Colorado Springs, Colorado, US.
5. SMITH, M.D., PEARL, J.C., CONRATH, B.J. and CHRISTENSEN, P.R. Thermal emission spectrometer results: Mars atmospheric thermal structure and aerosol distribution, *J Geophysical Research*, 2001, **106**, (E10), pp 23929-23945.
6. RAFKIN, S.C.R. and MICHAELS, T.I. Meteorological predictions for 2003 Mars exploration rover high-priority landing sites, *J Geophysical Research*, 2003, **108**, (8091), pp 1-23.
7. FUJITA, K., MOTODA, T. and NAGAI, H. Numerical analysis for an aerial deployment motion of a folded-wing airplane, Proceedings of the AIAA SciTech2014, AIAA 2014-0383, January 2014, National Harbour, Maryland, US.
8. FUJITA, K., MOTODA, T. and NAGAI, H. Dynamic behaviour of Mars airplane with folded-wing deployment, *Transactions of JSASS Aerospace Tech Japan*, 2014, **12**, No. ists29, pp Pk_1-Pk_6.
9. FUJITA, K., MOTODA, T. and NAGAI, H. Flow-coupled multibody dynamics simulation for an aerial deployment of a folded wing, Proceedings of the 10th International Conference on Flow Dynamics, OS13-54, November 2013, Sendai, Japan.
10. FUJITA, K., MOTODA, T. and NAGAI, H. Aerial-wing-deployment simulation of the folded-wing airplane with individual aerodynamic characteristics, Proceedings of the 2013 Asia-Pacific International Symposium on Aerospace Technology, 03-05-2p, November 2013, Takamatsu, Japan.
11. TAJIMA, H., *Fundamentals of Multibody Dynamics*, 2006, Tokyo Denki University Press, Tokyo, Japan (in Japanese).
12. OKAMOTO, M. and AZUMA, A. Aerodynamic characteristics at low Reynolds numbers for wings of various planforms, *AIAA J*, 2011, **49**, (6), pp 1135-1150.
13. HOERNER, S.F. and BORST, H. V. *Fluid-Dynamic Lift*, 1975, Hoerner Fluid Dynamics, Bricktown, New Jersey, US.
14. KATO, K., OYA, A. and KARASAWA, K. *Introduction to Aircraft Dynamics*, 1982, Tokyo University Press, Tokyo, Japan (in Japanese).
15 NASA, Glenn Research cCnter, Aerodynamics Index, Mars Atmosphere Model Metric Units, URL: http://www.grc.nasa.gov/WWW/K-12/airplane/atmosmrm.html [cited 16 November 2016].
16. SHAMPINE, L.F. and GORDON, M. K. *Computer Solution of Ordinary Differential Equations: the Initial Value Problem*, 1975, W.H. Freeman, San Francisco, California, US.
17. SHIMOYAMA, K., OYAMA, A. and FUJII, K.A. New efficient and useful robust optimization approach–design for multi-objective six sigma, Proceedings of the 2005 IEEE Congress on Evolutionary Computation, Vol. **1**, 2005, pp 950-957.
18. SHIMOYAMA, K., JEONG, S. and OBAYASHI, S. Methodology development and real-world application for multi-objective robust design, *J Reliability Engineering Association of Japan*, 2010, **32**, (2), (in Japanese), pp 105-112.
19. SHIMOYAMA, K. Robust aerodynamic design of Mars exploratory airplane wing with a new optimization method, PhD Dissertation, 2006, School of Engineering, University of Tokyo, Japan.
20. TAKEUCHI, S., YONEMOTO, K., IWATA, M., NARUMI, T., MATSUMOTO, T., FUKUDA, K., UCHIDA, J. and KATO, E. Conceptual structure design of Mars exploration airplane, Proceeding of the 49th Aircraft Symposium, JSASS-2011-5228, October 2011, Kanazawa, Japan (in Japanese).
21. NAGAI, H., OYAMA, A. and Mars Airplane WG. Development of Mars exploration aerial vehicle in Japan, Proceeding of the 30th International Symposium on Space Technology and Science, 2015-k-46, July 2015, Kobe, Japan.

https://doi.org/10.1017/aer.2016.123 Published online by Cambridge University Press